

DENSITY PROFILES OF Λ CDM CLUSTERS

ARGYRO TASITSIOMI¹, ANDREY V. KRAVTSOV¹, STEFAN GOTTLÖBER², ANATOLY A. KLYPIN³
Draft version August 14, 2018

ABSTRACT

We analyze the mass accretion histories (MAHs) and density profiles of cluster-size halos with virial masses of $0.6 - 2.5 \times 10^{14} h^{-1} M_{\odot}$ in a flat Λ CDM cosmology. We find that most MAHs have a similar shape: an early, merger-dominated mass increase followed by a more gradual, accretion-dominated growth. For some clusters the intense merger activity and rapid mass growth continue until the present-day epoch. In agreement with previous studies, we find that the concentration of the density distribution is tightly correlated with the halo's MAH and with its formation redshift. During the period of fast mass growth the concentration remains approximately constant and low $c_v \approx 3 - 4$, while during the slow accretion stages the concentration increases with decreasing redshift as $c_v \propto (1+z)^{-1}$. We consider fits of three widely discussed analytic density profiles to the simulated clusters focusing on the most relaxed inner regions. We find that there is no unique best fit analytic profile for all the systems. At the same time, if a cluster is best fit by a particular analytic profile at $z = 0$, the same is usually true at earlier epochs out to $z \sim 1 - 2$. The local logarithmic slope of the density profiles at 3% of the virial radius ranges from -1.2 to -2.0 , a remarkable diversity for the relatively narrow mass range of our cluster sample. Interestingly, for all the studied clusters the logarithmic slope becomes shallower with decreasing radius without reaching an asymptotic value down to the smallest resolved scale ($\lesssim 1\%$ of the virial radius). We do not find a clear correlation of the inner slope with the formation redshift or the shape of the halo's MAH. We do find, however, that during the period of rapid mass growth the density profiles can be well described by a single power law $\rho(r) \propto r^{-\gamma}$ with $\gamma \sim 1.5 - 2$. The relatively shallow power law slopes result in low concentrations at these stages of evolution, as the scale radius where the density profiles reaches the slope of -2 is at large radii. This indicates that the inner power law like density distribution of halos is built up during the periods of rapid mass accretion and active merging, while outer steeper profile is formed when the mass accretion slows down. To check the convergence and robustness of our conclusions, we resimulate one of our clusters using eight times more particles and twice better force resolution. We find good agreement between the two simulations in all of the results discussed in our study.

Subject headings: cosmology: theory – dark matter – clusters: formation – clusters – structure methods: numerical

1. INTRODUCTION

During the last decade, there has been an increasingly growing interest in testing the predictions of variants of the cold dark matter models (CDM) on small scales. The interest was spurred by indications that the density distribution in the inner regions of dark matter halos predicted by CDM is at odds with the observed galactic rotation curves (Flores & Primack 1994; Moore 1994). This discrepancy is yet to be convincingly resolved and is still a subject of active debate (e.g., Côté et al. 2000; van den Bosch & Swaters 2001; Blais-Ouellette et al. 2001; de Blok et al. 2001, 2003; Swaters et al. 2003). In addition, the CDM models face other apparent discrepancies with observations on galactic scales such as the amount of substructure in galactic halos (Klypin et al. 1999; Moore et al. 1999a), the incorrect normalization of the Tully-Fisher relation, the angular momentum of disk galaxies (Navarro & Steinmetz 1997, 2000), the ellipticity of dark matter halos (Ibata et al. 2001), and others.

In the past several years, the density distribution in the cores of galaxy clusters has also become a subject of a related debate. CDM models predict cuspy density profiles without flat cores (Frenk et al. 1985; Quinn et al. 1986; Dubinski & Carlberg 1991). Navarro et al. (1996, 1997, NFW) argued that the

CDM halo profiles can be described by the following simple formula in all cosmologies and at all epochs,

$$\rho(r) = \frac{\rho_0}{(r/r_s)(1+r/r_s)^2}. \quad (1)$$

This analytic formula describes the density profile of a halo using two parameters: a characteristic density, ρ_0 , and a scale radius, r_s . These parameters are determined by the halo virial mass, M_v , and concentration index, $c \equiv r_v/r_s$, where r_v is the virial radius of the halo. In addition, NFW argued that there is a tight correlation between c and M_v , which means that the halo profiles of different mass objects form a one parameter family.

Moore et al. (1998) (see also Ghigna et al. 2000) carried out a convergence study of the dark matter profiles and concluded that high mass resolution is required to resolve the inner density distribution robustly. They advocated the analytic density profile of the form $\rho(r) \propto (r/r_s)^{-1.5} [1 + (r/r_s)^{1.5}]^{-1}$, as a better description of the density distribution of their simulated halos. This profile behaves similarly to the NFW profile at large radii ($\propto r^{-3}$), but is steeper at small radii ($\propto r^{-1.5}$). Fukushima & Makino (1997, 2001, 2003) reached similar conclusions using a set of independent simulations. Jing & Suto (2000) presented a systematic study of the density profiles of halos with masses in the range $2 \times 10^{12} - 5 \times 10^{14} h^{-1} M_{\odot}$. They found that the inner slope at a radius of 1% of the virial radius is shallower (≈ -1.1) for cluster mass halos than for galactic halos (≈ -1.5). Recently, Hayashi et al. (2003); Navarro et al. (2003) found that often the logarithmic slope of the density distribution at the convergence radius is steeper than -1 as expected from the NFW profile, but significantly shallower than the -1.5

¹ Department of Astronomy and Astrophysics, Center for Cosmological Physics, The University of Chicago, Chicago, IL 60637; ired, andrey@oddjob.uchicago.edu

² Astrophysikalisches Institut Potsdam An der Sternwarte 16, 14482 Potsdam, Germany; sgottloeber@aip.de

³ Department of Astronomy, New Mexico State University, P.O. Box 30001, Las Cruces, NM, 88003; aklypin@nmsu.edu

inner slope found by Moore et al. (1998). Several other studies (Kravtsov et al. 1997, 1998; Avila-Reese et al. 1999; Jing 2000; Bullock et al. 2001; Klypin et al. 2001; Fukushige et al. 2003) found a significant scatter in both the shape of the density profiles and halo concentrations, likely related to the details of the mass accretion histories of individual objects (Wechsler et al. 2002; Zhao et al. 2003b). Mucket & Hoefft (2003) and Hoefft et al. (2004) study the radial dependence of the gravitational potential and the velocity dispersion and come to the conclusion that there does not exist a slope asymptote of the density profile over a wide range but the slope increases with decreasing radius and reaches the value -0.58 as $r \rightarrow 0$.

Observational constraints on the inner slope of the dark matter density distribution in galactic halos are difficult because the distribution is affected by the cooling and dynamics of baryons. The dark matter profiles in clusters, on the other hand, should be less affected by cooling as a much smaller fraction of cluster baryons is observed to be in the cold condensed phase. Observational studies of the mass distribution in clusters using weak lensing and hydrostatic analysis of the X-ray emitting gas show that the overall mass distribution is in general agreement with CDM predictions (Allen 1998; Clowe et al. 2000; Willick & Padmanabhan 2000; Clowe & Schneider 2001; Sheldon et al. 2001; Arabadjis et al. 2002; Athreya et al. 2003; Bautz & Arabadjis 2003).

Strong lensing studies can probe the mass distribution in the inner region of clusters and thus test the “cuspidity” of cluster halos. However, the results of strong lensing analyses have so far been contradictory, even in the case when the same system was studied. Tyson et al. (1998), for example, argue that the density profile of cluster CL0024+1654 has a constant density core, while Broadhurst et al. (2000) find that the mass distribution in this cluster is cuspy. Czoske et al. (2002) argue that CL0024+1654 is undergoing a major merger and its density profile may not be representative. Sand et al. (2002) find that the inner slope of the density profile in cluster MS2137–23 is flatter than expected in CDM models, a conclusion they recently confirmed for six more clusters (Sand et al. 2003). Gavazzi et al. (2002), reanalyzing the same observations, argue that if the fifth demagnified image near the center of the lensing potential is not taken into account then the inner slope may be consistent with CDM predictions.

Given the disagreement among the different analytical fits proposed for the density profiles of dark matter halos found in simulations and a possible discrepancy with strong lensing observations, it is interesting to conduct a systematic study of the density profiles of clusters in the concordance Λ CDM model. The study of cluster mass halos is also interesting because the typical concentrations of their matter distribution are lower than those of galactic halos. Thus, if an asymptotic inner slope, suggested by the analytic profiles, does exist it should be reached at a larger fraction of the virial radius in cluster halos and should be easier to detect.

The paper is organized as follows. In the following two sections, we describe the numerical simulations and halo finding algorithm used in our analysis. In § 4 we discuss the mass accretion histories of the analyzed clusters. In § 5 we present the convergence test, discuss the fitting procedure, and our results on the shapes and inner slopes of the density profiles. We summarize our results and conclusions in § 6.

2. NUMERICAL SIMULATIONS

We use the Adaptive Refinement Tree code (Kravtsov et al. 1997) to follow the evolution of cluster-size halos in the flat Λ CDM cosmology: $(\Omega_m, \Omega_\Lambda, h, \sigma_8) = (0.3, 0.7, 0.7, 0.9)$. We use the initial spectrum in the Holtzman approximation with $\Omega_b = 0.03$ (see Klypin & Holtzman 1997). The code starts with a uniform 256^3 grid covering the entire computational box. This grid defines the lowest (zeroth) level of resolution. Higher force resolution is achieved in the regions corresponding to collapsing structures by recursive adaptive refinement of all such regions. Each cell can be refined or de-refined individually. The cells are refined if the particle mass contained within them exceeds a certain specified threshold value. The code thus refines to follow the collapsing objects in a quasi-lagrangian fashion.

The cluster halos were simulated in a box of $80h^{-1}$ Mpc. A low resolution simulation was run first. A dozen cluster halos were identified and multiple mass resolution technique was used to set up initial conditions (Klypin et al. 2001). Namely, a lagrangian region corresponding to a sphere of radius equal to two virial radii around each halo was re-sampled with the highest resolution particles of mass $m_p = 3.16 \times 10^8 h^{-1} M_\odot$, corresponding to an effective number of 512^3 particles in the box, at the initial redshift of the simulation ($z_i = 50$). The high mass resolution region was surrounded by layers of particles of increasing mass with a total of three particle species. Only regions containing highest resolution particles were adaptively refined and the threshold for refinement was set to correspond to a mass of 4 highest resolution particles per cell. Each cluster halo is resolved with $\sim 10^6$ particles within its virial radius at $z = 0$. The size of the highest refinement level cell was $1.2h^{-1}$ kpc. In addition, one of the clusters was re-simulated with eight times more particles ($m_p = 3.95 \times 10^7 h^{-1} M_\odot$) to study the convergence of the density profiles. In this simulation, the smallest cell size reached was $0.6h^{-1}$ comoving kpc.

The time steps were chosen so that no particle moves by more than a fraction of the parent cell size in a single step. This criterion was motivated by the convergence studies presented by Klypin et al. (2001). For the analyzed simulations, the number of steps at the highest refinement level was ≈ 250000 or $\Delta t \approx 2 - 3 \times 10^4$ yrs and a factor of 2 larger for each lower refinement level. For the high-resolution resimulation of one of the cluster used for convergence check, the number of steps at the highest refinement level was ≈ 500000 . We analyze the cluster profiles and their mass accretion histories using 19 outputs from $z = 10$ to $z = 0$, with a typical time interval between outputs of ~ 0.7 Gyr.

3. HALO IDENTIFICATION

To identify cluster halos we use a variant of the Bound Density Maxima (BDM) halo finding algorithm. The main idea of the BDM algorithm is to find positions of local maxima in the density field smoothed at a certain scale and to apply physically motivated criteria to test whether the identified site corresponds to a gravitationally bound halo. The detailed description of the algorithm is given in Klypin & Holtzman (1997) and Klypin et al. (1999).

We start by calculating the local overdensity at each particle position using the SPH smoothing kernel⁴ of 24 particles. We then sort particles according to their overdensity and use all particles with $\delta \geq \delta_{\min} = 5000$ as potential halo centers. Starting with the highest overdensity particle, we surround each poten-

⁴ To calculate the density we use the publicly available code `smooth`: <http://www-hpcc.astro.washington.edu/tools/tools.html>

TABLE 1
SIMULATED HALO PARAMETERS

Halo	M_{180} ($h^{-1} M_{\odot}$)	r_{180} ($h^{-1} \text{Mpc}$)	V_{max} (km s^{-1})
CL1	2.5×10^{14}	1.58	973
CL2	2.4×10^{14}	1.56	1011
CL3	2.3×10^{14}	1.55	904
CL4	1.3×10^{14}	1.29	826
CL5	1.3×10^{14}	1.27	798
CL6	1.2×10^{14}	1.25	785
CL7	1.2×10^{14}	1.23	587
CL8	1.2×10^{14}	1.23	695
CL9	9.7×10^{13}	1.16	630
CL10	8.6×10^{13}	1.11	597
CL11	8.1×10^{13}	1.09	670
CL12	8.1×10^{13}	1.09	758
CL13	7.3×10^{13}	1.05	607
CL14	5.8×10^{13}	0.98	603

tial center by a sphere of radius $r_{\text{find}} = 50h^{-1}$ kpc and exclude all particles within this sphere from further center search. After all the potential centers are identified, we analyze the density distribution and velocities of the surrounding particles to test whether the center corresponds to a gravitationally bound clump (Klypin et al. 1999). We then construct profiles using only bound particles and use them to calculate the properties of halos such as the maximum circular velocity V_{max} , the mass M , etc. In this study, we consider only isolated cluster-size halos. We should note that for isolated halos the BDM algorithm works very similarly to the commonly used spherical overdensity (SO) algorithm.

The virial radius is a convenient measure of the halo size. We define the virial radius as the radius within which the density is equal to 180 times the *average* density of the universe at a given epoch. The separation between halos is sometimes smaller than the sum of their virial radii. In such cases, the definition of the outer boundary of a halo and its mass are somewhat ambiguous. To this end, in addition to the virial radius, we estimate the truncation radius, r_t , at which the logarithmic slope of the density profile constructed from the bound particles becomes larger than -0.5 as we do not expect the density profile of the CDM halos to be flatter than this slope. In general we consider the halo radius to be $r_h = \min(r_{180}, r_t)$.

In our analysis we use only clusters with masses $> 5 \times 10^{13} h^{-1} M_{\odot}$. In most cases two or more clusters were identified with this mass threshold in each run. To distinguish between the isolated cluster halos and massive subhalos we use additional information, such as the virial-to-tidal radius ratio, the maximum circular velocity, and the number of gravitationally bound particles within r_h . We consider halos to be isolated if their separation is larger than one third of the sum of their virial radii. We list the present-day properties of the cluster halos included in our sample in Table 1. The masses and radii correspond to the cumulative overdensity of 180 times the mean density of the Universe. In this list, clusters 4/12 and 10/13 are

close pairs, clusters 6/11/14 and 7/8/9 are triplets, while clusters 1, 2, 3, and 5 are well-isolated systems. The clusters thus sample a variety of environments.

We stress that the clusters in the analyzed sample were selected randomly – no specific criterion of relaxation or substructure was used. As the Figure 1 below shows clusters in our sample span a wide range of mass accretion histories and formation redshifts.

4. MASS ACCRETION HISTORIES

In the hierarchical structure formation scenario halos are assembled via a continuous process of merging and accretion. Details of the mass accretion history (MAH) may affect the shape of the halo and its density distribution (Navarro et al. 1997; Bullock et al. 2001; Wechsler et al. 2002; Zhao et al. 2003b). It is therefore interesting to study the accretion history of the halos in conjunction with the study of their density profiles. In this section we study the details of the assembly of the simulated cluster halos by following the most massive progenitor from $z = 10$ up to the present. We will discuss connections between the halo density profile and its MAH in § 5.3 and 6.

4.1. Constructing MAHs

For each $z = 0$ cluster halo we identify the most massive progenitor using the halo catalogs of the previous time output. In what follows, if halo 1 is the most massive *progenitor* of halo 2, then halo 2 will be referred to as the *offspring* of halo 1. To identify the most massive progenitor of a halo we first identify all of its progenitors in the halo catalog. We then eliminate from the set of potential progenitors, objects that are significantly tidally stripped (i.e., their virial-to-tidal radius ratio is greater than 3.5). We use the following criteria to identify the most massive progenitor among the remaining candidates. 1. We eliminate candidate progenitors with masses less than 20% of the offspring mass. 2. Using the peculiar velocity of the offspring, we find the approximate location of the progenitor in the previous output and eliminate the candidates outside the sphere with radius $r = 10 \times v_p \Delta t$, where v_p is the offspring peculiar velocity and Δt the time elapsed between two successive outputs. 3. We require that candidate progenitor and offspring halos have a certain fraction of common particles. In what follows, f_1 (f_2) denotes the ratio of the number of particles that offspring and progenitor have in common to the number of particles in the offspring (progenitor).

The candidate with the largest number of common particles with the offspring and with $f_1 \geq 0.5$ is then chosen to be the most massive progenitor. At the same time the condition $f_2 \geq 0.5$ is also checked and found to be satisfied. If all the progenitors have $f_1 < 0.5$, as is often the case during major mergers, for the progenitor with the largest f_1 we also require that more than 95% of the particles within a comoving radius of $10 h^{-1}$ kpc from the most bound particle of the progenitor are also found in the offspring. Starting from $z = 0$, we repeat the identification of the most massive progenitor for all the 19 simulation output epochs to $z \simeq 10$, or until the progenitor can no longer be identified. The mass accretion histories constructed in this way for each of the analyzed clusters are shown in Figure 1 (solid lines).

Most of the MAHs have a qualitatively similar shape: a rapid increase in mass during the early epochs and a relatively slow increase at the later stages of evolution. Despite the similarities, the details of MAHs differ significantly from object to object. CL9, CL10, and CL13 have not yet reached the second,

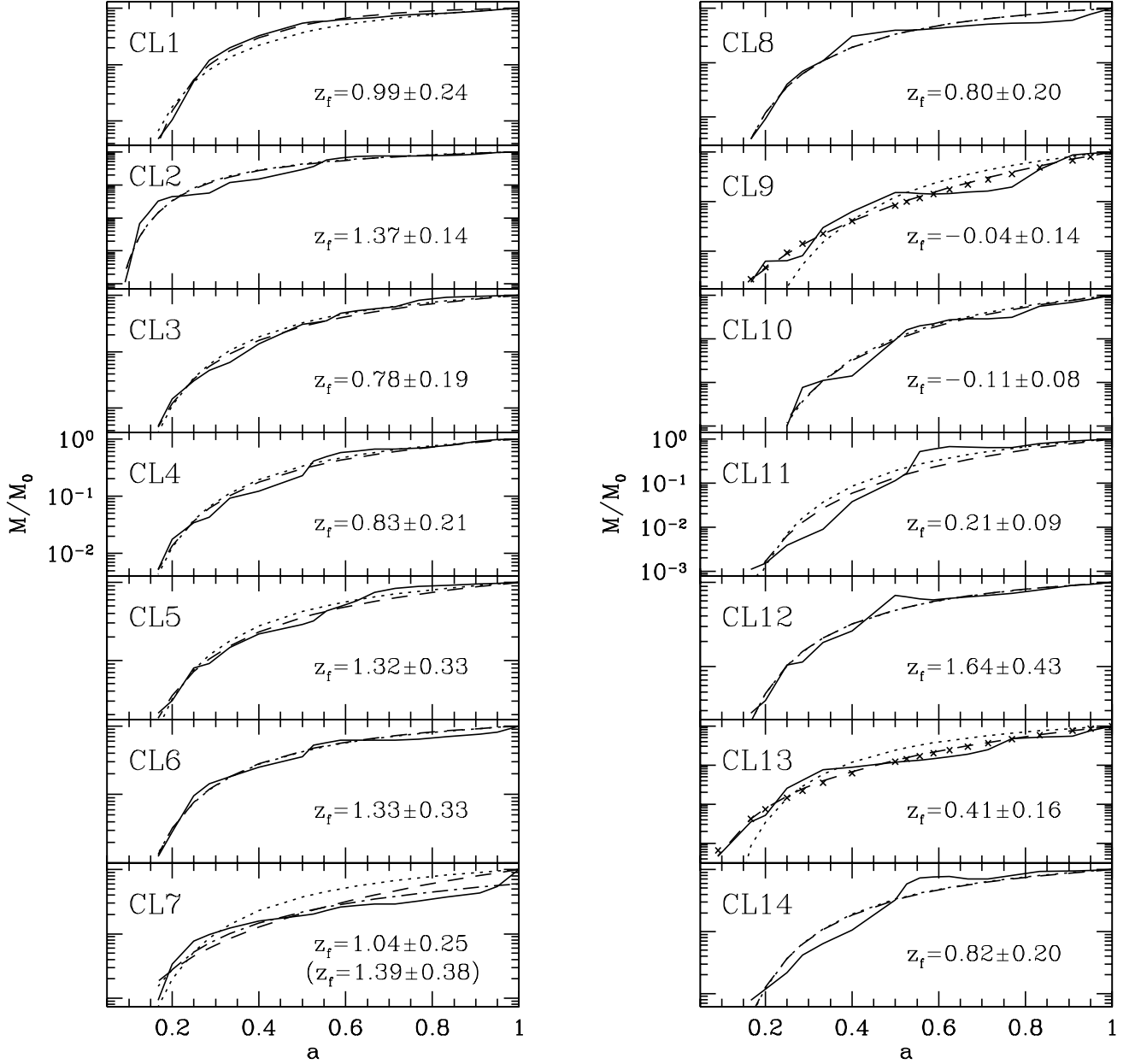


FIG. 1. — Mass accretion histories of the cluster halos (*solid lines*). Also shown are the analytic fits of Eq. (4), $M(\tilde{a})/M_0 = \tilde{a}^p \exp[-\alpha(\tilde{a}-1)]$ (where $\tilde{a} \equiv a/a_0$, and $a = (1+z)^{-1}$). The *dashed lines* show fits with both α and p varied, while the *dotted lines* show the fits with the parameter p fixed to zero. The formation redshift z_f , given by Eq. (3) in terms of α , is shown in the legend of each panel. The best fit α obtained from the two fits is nearly identical in all cases, except for CL9 and CL13. For CL9 and 13 we also plot the fit obtained using Eq. (5) (*crosses*). Finally, to show the effect of a recent major merger, for CL7 we plot the fit assuming an epoch of observation $a_0 = 0.95$ rather than $a_0 = 1$, used for all the other fits (*dash-dotted line*). The z_f value obtained in this case is given in the parentheses.

accretion dominated stage of their evolution. Their mass is accumulated via intense merger activity up to the present epoch. CL7 and CL8 appear to have reached the slow accretion phase, but experienced a late major merger. The masses of CL11 and 14 at early epochs increase almost linearly with the expansion factor ($\log(M/M_0) \propto a$), and reach a $M \approx \text{const}$ plateau at later epochs.

4.2. Major mergers

In addition to the overall shape of the halo MAH, it is useful to have some more specific information on the major mergers experienced by the clusters. We will use the term *major merger* to describe all events that result in a more than 30% increase in the mass of the main progenitor between the two output epochs. As we mentioned above, the average time elapsed between two successive outputs of the simulation is ≈ 0.7 Gyr, which is close to the crossing time of ≈ 1 Gyr for a wide range of halo masses. The crossing time is a lower limit for the merger time scale, which means that the spacing of our outputs is appropriate for merger identification (see also tests in Gottlöber et al. 2001). We tabulate the redshift of the last major merger, z_{LMM} , as well as the corresponding fractional mass change, $\Delta M/M$, for all the clusters in columns 2 and 3 of Table 2, respectively. One should keep in mind that these numbers are only indicative, since defining a major merger, e.g., as a 20% mass increase, would render z_{LMM} for CL4 equal to $\simeq 0.15$.

4.3. Formation redshift and MAH shape

To characterize evolution of the halos, one can introduce the halo formation epoch (or redshift). Usually, the formation epoch is defined as the time when the mass in the most massive progenitor(s) is equal to some fraction of the halo's final mass, M_0 (e.g., see Lacey & Cole 1993; Navarro et al. 1997). Taking this fraction to be equal to $1/2$ we calculate the formation redshift, $z_{1/2}$, which we tabulate in column 4 of Table 2. In order to find $z_{1/2}$ we use linear interpolation between the successive outputs that bracket $M/M_0 = 1/2$. It is interesting to note that $z_{1/2}$ is typically smaller than z_{LMM} .

As pointed out by Wechsler et al. (2002, hereafter W02), defining the formation redshift as the redshift where the ratio M/M_0 takes a specific value gives a formation redshift that depends on the time of observation of the halo. In addition, the definition uses the MAH of the halo at two epochs only (the formation and present epochs) and therefore makes it sensitive to the local jumps in the MAH and less sensitive to the overall MAH shape. The case of CL7 may serve as an illustration. This object had entered its quiescent stage of evolution relatively early. Nevertheless, the low value of its formation redshift, $z_{1/2}$, is determined largely by the single late major merger. In view of these considerations, W02 argued that the mass accretion histories can be better characterized by a formation redshift that is derived from a functional fit to the entire MAH. Namely, they propose to fit the MAHs of halos by a simple exponential:

$$\tilde{M}(\tilde{a}) = \exp[\alpha(1-1/\tilde{a})]; \quad \tilde{a} \equiv a/a_0; \quad a = (1+z)^{-1}, \quad (2)$$

where $\tilde{M} \equiv M/M_0$, and M_0 and a_0 are the virial mass of the halo and expansion factor at the epoch of observation, respectively. Using the fit, one can define the formation epoch independent of the epoch of observation as the redshift corresponding to a fixed value of $d \log M / d \log a = S$. The value of S is arbitrary, and we follow W02 and choose $S = 2$ since this is the value required to match the concentration index-collapse redshift relation found

by Bullock et al. (2001). The formation redshift, z_f , can then be defined by the relation

$$z_f = \frac{2}{\alpha}(1+z_0) - 1. \quad (3)$$

The formation redshift in this definition is independent of the epoch of observation; the factor $(1+z_0)$ appears only in order to comply with the convention of $z = 0$ corresponding to the present epoch.

Although the simplicity of the above expression is attractive, we find that in some cases it provides a rather poor fit to the individual MAHs. We generalize the fitting formula by the following two-parameter function

$$\tilde{M}(\tilde{a}) = \tilde{a}^p \exp[\tilde{\alpha}(1-1/\tilde{a})], \quad (4)$$

The function in Eq. (2) is a special case of Eq. (4) for $p = 0$. The fits in which both α and p were varied and the fits with fixed $p = 0$ are shown in Figure 1. These fits were obtained by χ^2 minimization, even though the robustness of their relative quality with respect to the choice of merit function was tested. For CL9 and 13 the fits with $p = 0$ are rather poor. For the two-parameter fits to the MAHs of these clusters the value of $\tilde{\alpha}$ is close to zero, which means that the MAHs are better described by a power law in \tilde{a} , rather than by an exponential in $1/\tilde{a}$. Detailed study of the MAH shapes clearly requires a larger sample of halos. Analyzing the merger histories in terms of number of major mergers indicates that the power law behavior may be related to the high frequency of major mergers up to the present epoch. We note that the *galaxy-size* halos studied by W02 formed earlier on average than our halos, and thus only a small fraction ($< 5\%$) of their halos were similar to our CL9 and 13.

Clearly, a smooth fitting function for the MAHs cannot capture all the features of the actual evolution, such as minor and major merger events. These events however do influence the values of the best fit parameters. In the case of CL7, one can see the effect of a very recent major merger. As can be seen in Figure 1, if we make the fit at $a_0 = 0.95$ instead of $a_0 = 1$ (i.e., with the observation epoch prior to the merger), we get a better overall fit.

van den Bosch (2002) found that the *average* mass accretion history of halos generated using the extended Press-Schechter (EPS) formalism is described well by a different two-parameter function

$$\log(\tilde{M}) = -0.301(-1)^\nu \left[\frac{\log(a)}{\log(1+\tilde{z}_f)} \right]^\nu, \quad (5)$$

with \tilde{z}_f, ν the parameters to be determined. By definition, \tilde{z}_f is the redshift which corresponds to $\langle M/M_0 \rangle = 1/2$. Typical best fit values for ν are in the range of 1.4–2.3. As before, clusters CL9 and 13 are exceptions with $\nu \approx 1$ (i.e., their MAH is power-law $M \approx M_0 a^\nu$). We find that Eq. (5) gives fits equally good to those obtained with the two-parameter function of Eq. (4) in all cases. This function however is not convenient when used to calculate the formation redshift via the logarithmic derivative of the mass with respect to the scale factor. More specifically, in Eq. (5) (and its derivative) \tilde{z}_f is by construction positive, and thus for a general ν , a has to be ≤ 1 . This will not be the case for objects whose mass accretion rate reaches $S = 2$ in the future (negative formation redshift), and thus Eq. (5) cannot be used in these cases to obtain a formation redshift. We choose to use Eq. (4), as it is a simple extension of the function used by W02 and the definition of z_f via the mass logarithmic derivative is guaranteed.

TABLE 2
HALO PARAMETERS FROM MASS ACCRETION HISTORIES AND DENSITY FITS

Halo (1)	z_{LMM} (2)	$\Delta M/M$ (3)	$z_{1/2}$ (4)	z_f (5)	Best fit (6)	c_{-2} (7)	slope (8)
CL1	1.24	0.65	1.09	0.99 ± 0.24	M	9.7	-1.23 ± 0.19
CL2	0.85	0.56	0.83	1.37 ± 0.14	JS	9.6	-1.67 ± 0.15
CL3	0.75	0.36	0.67	0.78 ± 0.19	NFW	10.7	-1.35 ± 0.20
CL4	0.95	0.77	0.78	0.83 ± 0.21	JS	5.4	-1.89 ± 0.20
CL5	0.85	0.34	0.69	1.32 ± 0.33	M	12.2	-1.30 ± 0.20
CL6	0.95	0.45	0.91	1.33 ± 0.33	JS	14.7	-1.83 ± 0.19
CL7	0.03	0.82	0.07	1.04 ± 0.25	JS	13.6	-2.01 ± 0.22
CL8	1.74	1.83	0.41	0.80 ± 0.20	M	11.5	-1.25 ± 0.22
CL9	0.15	0.95	0.19	-0.04 ± 0.14	M	3.5	-1.68 ± 0.22
CL10	0.25	0.78	0.22	-0.11 ± 0.08	M	2.3	-1.78 ± 0.28
CL11	0.85	2.11	0.80	0.21 ± 0.09	NFW	8.4	-1.38 ± 0.31
CL12	1.24	1.67	1.23	1.64 ± 0.43	M	12.6	-1.50 ± 0.24
CL13	0.03	0.33	0.25	0.41 ± 0.16	JS	4.3	-1.36 ± 0.42
CL14	0.95	0.81	0.93	0.82 ± 0.20	JS	10.8	-1.42 ± 0.30

Note. — (2): redshift of last major merger, (3): fractional mass change during last major merger, (4): redshift where half of the cluster’s current mass has been accreted, (5): formation redshift defined from MAHs, (6): best fit among the Navarro et al. (1996, 1997), the Moore et al. (1998), and the Jing & Suto (2000) profiles (7): concentration index, (8): logarithmic slope as obtained by averaging the local logarithmic slope between the smallest resolved radius and 3% of the virial radius

The formation redshifts estimated using the best fit parameters of Eq. (3) and Eq. (4) are given in column 5 of Table 2. Note that this definition of z_f allows for future (negative) formation redshifts. The two definitions of the formation redshift, $z_{1/2}$ and z_f , are correlated at 98% probability level (a Spearman rank correlation of 0.58). In addition, to evaluate the effect of the early and late portions of the MAH on the formation redshift, we estimated the formation redshifts using only the parts of the MAH for which $a < 0.65$ and $a > 0.65$: $z_f^{<0.65}$ and $z_f^{>0.65}$. The best fit values of both $z_f^{<0.65}$ and $z_f^{>0.65}$ are consistent with the values of z_f within errors. In addition the values of $z_f^{>0.65}$ are consistent with $z_f^{<0.65}$ within (large) errors. Although our cluster sample is small, the significant spread in the values of z_f for clusters of the same M_{180} is apparent. This indicates that halos of the same mass exhibit a wide range of MAH shapes.

5. DENSITY PROFILES

5.1. The fitting procedure

For each cluster halo, we fit the Navarro et al. (1997, NFW), the Moore et al. (1998, M), and the Jing & Suto (2000, JS) analytic density profiles. For a general profile of the form

$$\rho(r) = \frac{\rho_s}{x^\gamma(1+x^\alpha)^{(\beta-\gamma)/\alpha}}, \quad x \equiv r/r_s, \quad (6)$$

the NFW, M, and JS profiles have values of (α, β, γ) : (1, 3, 1), (1.5, 3, 1.5), and (1, 3, 1.5), respectively.

In what follows, we will define the concentration of a halo as $c_{-2} \equiv r_{180}/r_{-2}$ and $c_v \equiv r_{vir}/r_{-2}$, where r_{-2} is the radius where the logarithmic slope of the best fit profile is equal to -2, r_{180} is the radius within which the average density is equal to 180 times the *mean* matter density of the universe, and r_{vir} is the

virial radius defined using the redshift-dependent virial overdensity (≈ 180 at $z > 1$ and ≈ 340 at $z = 0$). To convert from (M_{180}, r_{180}) to (M_{vir}, r_{vir}) we use the fitting formulas of Hu & Kravtsov (2003). For the general profile of Eq. (6), the radius r_{-2} is given by

$$r_{-2} = \left(\frac{\gamma-2}{2-\beta} \right)^{1/\alpha} r_s, \quad (7)$$

where r_s is the scale radius of the corresponding analytic profile. Thus, $r_{-2} = r_s$ (NFW), $r_{-2} \approx 0.63r_s$ (M), $r_{-2} = 0.5r_s$ (JS). In other words, $c_{-2} = c_{NFW}$, $c_{-2} \approx 1.59c_M$, and $c_{-2} = 2c_{JS}$, if the best fit is found to be the NFW, the M, or the JS profile, respectively. We present the resulting concentration indices at $z = 0$ in column 7 of Table 2.

There is a number of factors that may affect the fits of analytic profiles to the profiles of the simulated clusters: the choice of binning, the merit function, the range of radii used in the fitting, the weights assigned to the data points, etc. For example, for the merit functions sensitive to the number of bins, such as χ^2 , the choice of binning and bin weights are extremely important.

In the following analysis, we use equal-size logarithmic bins in order to give more statistical weight to the inner regions of the halos. The number of bins is thirty for late epochs. For early epochs the number of bins is reduced to ensure that each bin contains a sufficiently large number (> 100) of particles. We take as bin center the average radius of all particles in a bin. We checked that the fits are robust when varying the number of bins around the adopted value. We find, however, that the choice of binning affects the quality of the fit. For example, for a large number of bins the resulting profiles are quite noisy. Our choice of binning minimizes the noise. We weight the data points by the poisson noise in the number of particles of each

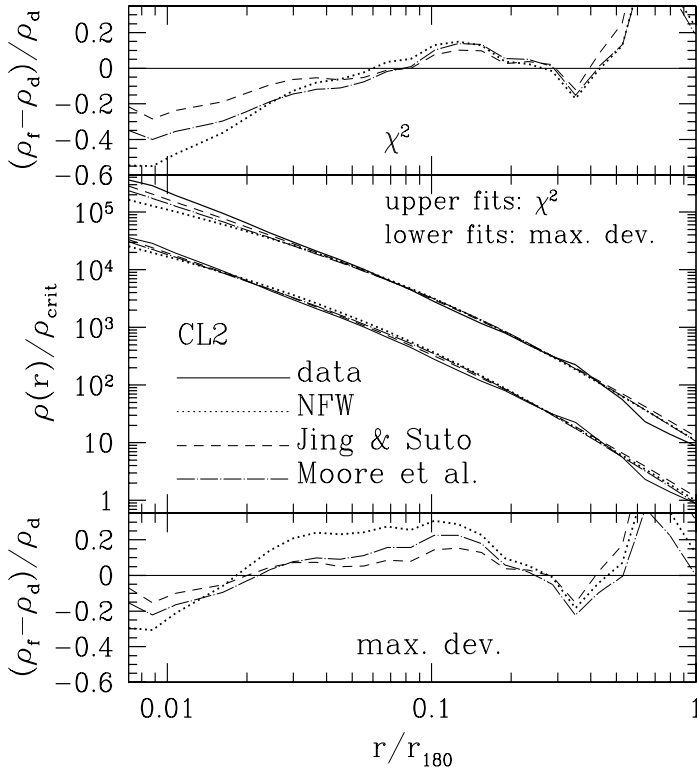


FIG. 2.— *Middle panel*: NFW (dotted lines), Jing and Suto (short-dashed lines), and Moore et al. (dot-dashed lines) fits to the density distribution of CL2 (solid lines). The upper set of lines corresponds to results obtained by a χ^2 minimization and the lower set (displaced by a factor of 10 for clarity) to fits obtained by minimizing the maximum absolute fractional deviation of the fits from the data. *Upper panel*: Fractional deviation of the fits (ρ_f) from the data (ρ_d) for fits obtained via χ^2 minimization. *Lower panel*: Same as in the upper panel but for fits obtained via maximum absolute fractional deviation minimization.

bin.

The presence of substructure may substantially bias fits of smooth analytic profiles. In particular, substantial amount of substructure is present in the outer regions of halos and the profiles in these regions are often non-monotonic exhibiting “bumps”. To minimize the bias, we fit the profiles using only the bins from a minimum resolved radius (see § 5.2) up to the radius within which the average density is equal to 500 times the *critical* density of the universe, r_{500} . This choice is motivated by the results of Evrard et al. (1996) who find that the material within this radius is generally relaxed and in hydrostatic equilibrium. We find that for the clusters in our sample $r_{500}/r_{180} \simeq 0.36-0.37$ at $z=0$. To the same end, the density profiles of CL9 and 10 were obtained by averaging the $z=0$ and $z \approx 0.05$ outputs. This renders the profiles less noisy and improves the quality of the obtained fits. The averaging does not change the best fit parameters significantly.

It is important to understand that the formal quality of the fit may depend on the merit function, as well as the kind of binning and weighting used. In the following analysis, we fit the analytic profiles for the parameters ρ_s and r_s by minimizing the χ^2 . Klypin et al. (2001) show that χ^2 merit function applied to the profiles with logarithmic binning with the Poisson error weights results in the fits of the NFW profile that are systematically below the simulated profiles in the inner regions. The logarithmic binning gives higher density of data points at small radii, creating thus bins with smaller number of particles. The χ^2 fits for the CL2 profile are shown in Figure 2.

Also shown are the fits obtained when using the maximum fractional deviation (MFD) merit function, $\max[|\rho_{\text{fit}} - \rho_{\text{data}}|/\rho_{\text{data}}]$, which gives equal weight to all radial bins. Figure 2 shows that this merit function reduces the deviations in the inner region ($r \lesssim 0.02r_{180}$) at the expense of significant deviations at intermediate radii ($0.02 \lesssim r/r_{180} \lesssim 0.2$). Although the MFD merit function is less sensitive to the choice of binning, it is more sensitive to the presence of substructure bumps in the profile than χ^2 . Both merit functions have their pluses and minuses.

Luckily, we find that regardless of the merit function and bin weighting used, the relative goodness of fits for different analytic profiles remains the same. If, for example, the M profile is a better fit to the simulated profile than the NFW and JS profiles in the χ^2 minimization, it is the resulting best fit in the maximum deviation minimization as well. The conclusion about which profile fits best is therefore robust. Note, however, that this is not true for the conclusions about the *systematic* ways by which a given fit fails. For example, the characteristic ‘S’ shape of the fractional deviation as a function of radius for the NFW fits found in various studies (e.g., Moore et al. 1999b; Ascasibar 2003) is not a robust result because it depends on the merit function, binning and weighting.

In addition to the three widely used analytic profiles, we experimented with fits of more general analytic expressions of the form given by Eq. (6). Overall, the fitting procedure with all three parameters α, β, γ varied leads to strong degeneracies between parameters (see also Klypin et al. 2001). One can find several combinations of parameters that fit the data equally well. For example, good fits with inner asymptotic inner slopes as shallow as $\gamma = -0.3$ can be found.

In view of these degeneracies, we choose not to use generalized fits but simply complement the analytic fits with measurements of the logarithmic slope profiles $s(r) \equiv \partial \log \rho(r) / \partial \log r$. This analysis is complementary to the fits because the slope is sensitive to the local shape of the profile, while the fits may be sensitive to its global shape. The logarithmic slope is computed using the linear fit to $\log \rho - \log r$ locally. We use five neighboring profile bins centered on a given bin in the fit (i.e., two bins on either side) with a total of 100 bins for the whole range of radii from r_{min} to r_{180} . The choice of the number of bins is a tradeoff between the slope errors and spatial resolution. We experimented with fitting polynomials up to the 4th order but found no advantage over a simple linear fit. The local logarithmic slope is sensitive to the presence of transient massive substructures within the halo. For illustrative purposes only, to reduce the substructure-induced noise, we additionally smooth the slope using a tophat filter.

5.2. Convergence Study

To study the effects of mass and force resolution, CL2 was resimulated with eight times more particles ($m_p = 3.95 \times 10^7 h^{-1} M_\odot$) and with more refinements. The ART code performs mesh refinements when the number of particles in a mesh cell exceeds a specified threshold. Thus, the mass resolution is tightly linked to the peak spatial resolution achieved in simulation. The cell size of the highest refinement level, which we will consider to be the formal resolution of the simulation, was $0.6h^{-1}$ kpc and $1.2h^{-1}$ kpc in the higher- (HR) and lower-resolution (LR) simulation, respectively. The HR simulation was initialized using the same set of modes as the LR. We therefore follow the formation of the same object with more particles. The comparison of density profiles allows us to check for the two-body relaxation

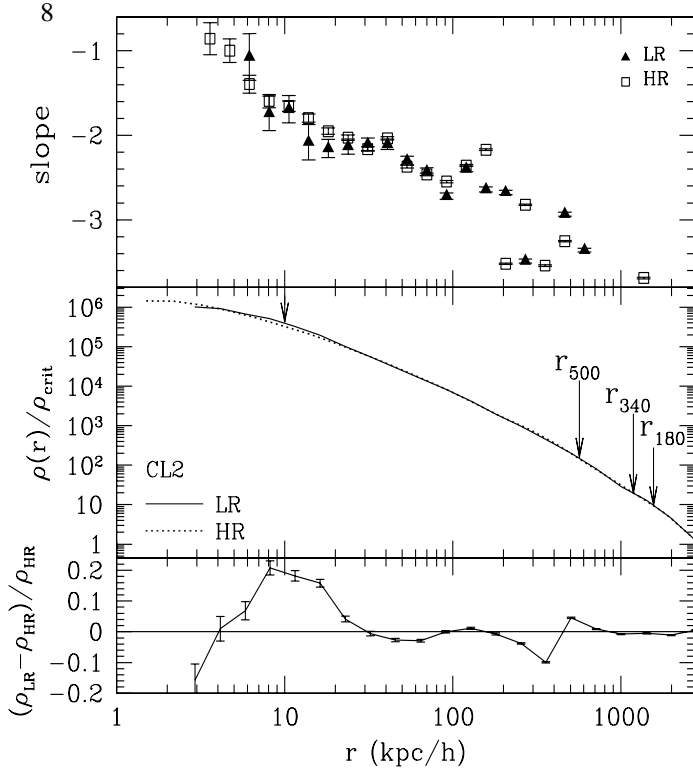


FIG. 3.— Density profiles of the cluster CL2 in the low- (LR, *solid line*) and high-resolution (HR, *dotted line*) simulations (*middle panel*). The profiles were obtained by averaging the $z = 0, 0.02$ and 0.1 outputs of the corresponding runs. The *bottom panel* shows the fractional deviation between the LR and HR profiles. The error bars are computed by propagating the shot noise in the density profiles. The *top panel* shows the local logarithmic slope as a function of radius in the HR (*squares*) and the LR (*triangles*) runs. In the middle panel, the vertical arrow at $\simeq 10h^{-1}$ kpc (or four times the formal resolution of the LR run) denotes the minimum distance used in our analyses. The arrows at large scales denote the radii corresponding to various commonly used overdensities: r_{500} , the radius within which the average density equals 500 the critical density, and r_{340} and r_{180} , the radii within which the average density equals 340 and 180 times the *mean* density of the universe, respectively.

effects, which may be important in cluster cores (Diemand et al. 2003), and numerical convergence.

We compare the density profiles of CL2 in the HR and LR simulations in Figure 3. In order to minimize the differences due to substructure, the profiles shown are obtained by averaging the $z = 0, 0.02$, and 0.1 outputs of the corresponding runs. The figure shows that the fractional difference between the profiles is $\lesssim 0.2$ down to ~ 3 formal resolutions of the LR run. This is in agreement with a previous convergence study for the ART code using simulations with lower mass resolution (Klypin et al. 2001). Comparison of density profiles of clusters in ART simulations with the density profiles in simulations using the Gadget code (Springel et al. 2001) was recently performed by Ascasibar et al. (2003), who found excellent agreement between the two codes at the resolved scales.

The upper panel of Figure 3 shows the local logarithmic slope of the density profiles as a function of radius (see § 5.1 for details). The error bars are computed by propagating the Poisson errors in the density profiles. At $r \gtrsim 200h^{-1}$ kpc the strong non-monotonic variations of the slope are due to the presence of substructure. Despite the averaging, the small differences in the locations of substructures result in large differences in the slope value at a given r . At the same time, the slopes in the HR and LR runs agree well at scales $5 \lesssim r \lesssim 200h^{-1}$ kpc. It is interesting to note that there is no evidence for a well-defined asymptotic

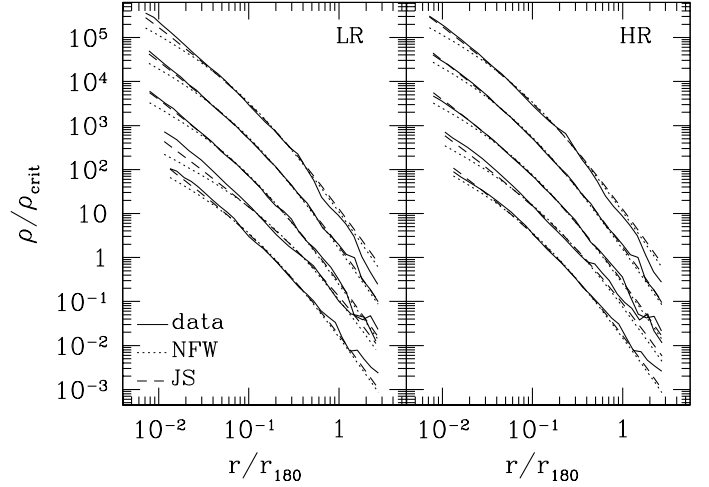


FIG. 4.— The density profile of CL2 at (from top to bottom) $z = 0, 0.2, 0.4, 1$, and 1.5 (*solid lines*), for the low (LR, *left panel*) and high (HR, *right panel*) resolution runs. The profiles at $z > 0$ are scaled down by a factor of 10 with respect to each other. Also shown are the best fit NFW (*dotted lines*) and the JS (*dashed lines*) profiles. The figure shows that at all shown redshifts the JS profile is a better fit to the simulated profiles than the NFW in both runs.

inner slope. The local logarithmic slope in both runs monotonically increases with decreasing radius down to the smallest resolved scales.

Based on these results, in the subsequent analysis we will conservatively consider only scales greater than $r_{\min} = 10h^{-1}$ comoving kpc or (eight formal resolutions of the LR run) for both the fits and the plots. In addition, we require that more than 200 particles are contained within the minimum radius (Klypin et al. 2001). In our simulations this criterion is relevant only at early epochs ($z \gtrsim 2$), since at later epochs a $10h^{-1}$ kpc radius always contains more than 200 particles for all clusters.

One of the main results of our analysis is an apparent diversity of the density profiles. At the same time, we find that if a profile is best fit by a particular analytic profile at $z = 0$, it is generally best fit by the same analytic profile at early epochs out to $z \sim 1 - 2$. Potentially, this is an interesting clue to the processes that determine the shape of the profile. It is therefore important to check that the conclusion does not change with resolution. Figure 4 shows the fits of the NFW and JS profiles to the profiles of CL2 in the LR and HR runs at different epochs. The fits were done using bins in the radial range $[r_{\min}, r_{500}]$ (see § 5.1). The figure shows that at all shown redshifts the JS profile fits the simulated profiles at small radii better than the NFW profile in both runs. This is remarkable as the cluster experiences fairly rapid increase in mass and several violent mergers between $z = 1.5$ and $z = 0$. The mass changes by more than a factor of five during this period (see Fig. 1). The cluster undergoes an intense merger event at $z \sim 0.6$ and the last major merger for our definition occurred at $z = z_{\text{LMM}} \simeq 0.85$.

We find that our fitting results are robust to changes in both the minimum and maximum radius used in the fits. For example, concentration changes by no more than $\simeq 10 - 20\%$ if a different outer radius is used ($\sim 2/3r_{180}$, and for some clusters an outer radius $\sim r_{180}$ did not change the results much). More importantly, the conclusion about the best fit analytic profile remains the same, although in some cases the best fit changes

from the M to the JS or vice versa. This can be expected because these analytic profiles are quite similar. We also repeated fits with twice as large minimum radius ($\approx 20h^{-1}$ kpc comoving) and find that the best fit analytic profile remains the same and that the concentration changes by $\lesssim 10\%$.

5.3. Results

Our results on the density profiles at $z = 0$ are presented in Figure 5. In the middle panel we plot the actual profiles as well as the NFW, M, and JS fits. All profiles are plotted at $r < r_{180}$ but are fit using only bins in the range $r_{\min} < r < r_{500}$, as discussed in § 5.2. In the lower panel we present the fractional deviation as a function of distance for each of the analytic fits. The analytic profile that provides the best fit to the profile of each cluster is given in column 6 of Table 2. In the upper panel we plot the logarithmic slope as a function of radius for each of the analytic fits and the actual local logarithmic slope as calculated from the simulated profiles (see § 5.1).

In most cases the best analytic fit provides by far the best fit compared to the other profiles. This is especially true for CL3 and 11 (see Fig. 5), the two clusters best fit by the NFW profile. The other two analytic profiles fail significantly compared with the NFW for these clusters. If we consider the similar M and JS as one family of profiles, the two families (NFW and M/JS) typically differ significantly in quality. As discussed above, the systematic way in which the NFW profile fails to fit the data can be attributed to the merit function used to obtain the fits. For our choice of merit function, the fits follow the actual profile well at intermediate distances. The largest deviations occur at the innermost regions. For large distances, the three fits are almost indistinguishable.

Figure 5 and Table 2 clearly show that there is significant dispersion in the shapes of the profiles, concentrations, and inner slopes. The dispersion of concentration parameter was studied in several analyses (Navarro et al. 1997; Jing 2000; Bullock et al. 2001; Eke et al. 2001; Wechsler et al. 2002; Zhao et al. 2003b) and is thought to be related to the distribution of the halo formation epochs (Wechsler et al. 2002). The typical values of scatter are $\sigma_{\log c_v} \approx 0.14$ with only a weak dependence on mass (Bullock et al. 2001; Wechsler et al. 2002). Table 2 shows that the c_{-2} concentration indices of our clusters span a wide range of values, from 2.3 to 14.7. Making the appropriate conversion from c_{-2} to c_v , we find that the formal dispersion is $\sigma_{\log c_v} \approx 0.2$ at $z = 0$, larger than the dispersion for the smaller mass halos used to derive this scattering in other studies, which may reflect the more recent formation times of cluster halos, as well as their more diverse MAHs. For example, Klypin et al. (2003) and Colin et al. (2003) find a significantly smaller dispersion $\sigma_{\log c_v} \approx 0.1$ for a subsample of relaxed halos without significant substructure. Indeed, the clusters with the three lowest concentrations, CL9, 10, and 13 have all had a recent major merger (see z_{LMM} in column 2 of Table 2). The small concentration of these objects is due to the shape of their density profiles which are close to a power law over a wide range of radii. Careful examination of MAHs and merger histories, indicates that the recent major merger activity results in a low concentration of density profiles. CL4, which also has a small concentration compared to the majority of the clusters, has a formal $z_{LMM} = 0.95$, for the definition of major merger adopted in our study. However, in agreement with the other low concentration objects, it had a large merger ($\approx 22\%$ fractional mass increase) at a very recent epoch ($z \approx 0.15$). In addition, we find a strong

correlation between z_f and c_{-2} , in agreement with the correlation advocated by W02.

Figure 6 shows the redshift evolution of the median virial concentration, c_v , of our sample. We also plot the predictions of the models by Bullock et al. (2001) and Eke et al. (2001). Our results seem to be in some general agreement with both model predictions. Overall, the Eke et al. (2001) seems to be in better agreement than the Bullock et al. (2001) model. Recently, Dolag et al. (2003) found that the standard Bullock et al. (2001) recipe systematically underestimates concentrations of cluster-size halos at all redshifts. Figure 6 shows a similar trend in our simulations, although the difference we find is noticeably smaller. This may be due to the smaller mean mass of clusters in our sample. Zhao et al. (2003b), for example, show that discrepancy between simulations and the Bullock et al. (2001) model increases with increasing halo mass. In the mass range probed here the difference from the analytic prescription of Bullock et al. (2001) is considerably smaller than the scatter in concentrations.

Figure 7 shows the evolution of the average concentration and the average MAH of our clusters. The figure shows that during the period of rapid mass growth the concentration is nearly constant at $c_v \approx 3-4$, while during the period of gradual mass growth it increases with decreasing redshift as $c_v \propto (1+z)^{-1}$. Therefore, the concentration of halos is approximately constant while they experience frequent major mergers and there may exist a ‘‘floor’’ to the concentration values of $c_{\min} \approx 3$, while concentrations start to increase with time at $z < z_f$. This behavior was pointed out by Zhao et al. (2003b,a). However, unlike Zhao et al. (2003b), we find that the model of Wechsler et al. (2002) does not underestimate the concentrations at the cluster-size halos of our sample. The evolution of average concentration in Figure 7 is similar to that found by Dolag et al. (2003). The mean concentration of cluster progenitors in their simulations (their Figures 4 and 7) is approximately constant at $z \gtrsim 1$.

We do not find a clear connection between the redshift of last major merger and the best fit profile (column 6 in Table 2). We do find that none of the objects with low z_{LMM} has the NFW profile as the best fit, but the statistics of our sample is too small to reach a firm conclusion. Nevertheless, for each individual system the shape of its density profile is remarkably stable during evolution. The best fit analytic profile at $z = 0$ is typically also the best fit at earlier epochs, as was shown for CL2 in Figure 4. Figure 8 shows evolution of the density profiles and the analytic fits at each epoch for CL1 and CL3. The NFW profile is a better fit than the JS at all epochs for $z < 1.5$ for CL1. This stability of the profile shape with time holds for most clusters with some exceptions. CL3 illustrates the case where the best fit analytic profile changes from epoch to epoch. We find this behavior for four out of the fourteen clusters in our sample.

Note that the NFW fits never reach their inner asymptotic slope of -1 at the radii we probe. The average logarithmic slopes estimated by averaging the local slope around $0.03r_{180}$ (see §5.1) range from -1.2 to -2, and are given in column 8 of Table 2. In most cases, the local slope changes monotonically with radius with no sign of reaching the asymptotic inner slope. Note that for typical concentrations of cluster halos we expect the asymptotic slope to be reached at the resolved scales, at least for the M profile⁵. This can be seen from the slope profiles for

⁵ From Eq. (6) r_s is the radius where the logarithmic slope is equal to $-(\beta+\gamma)/2$ with the asymptotic slope reached at $r \ll r_s$. The NFW and the JS profiles

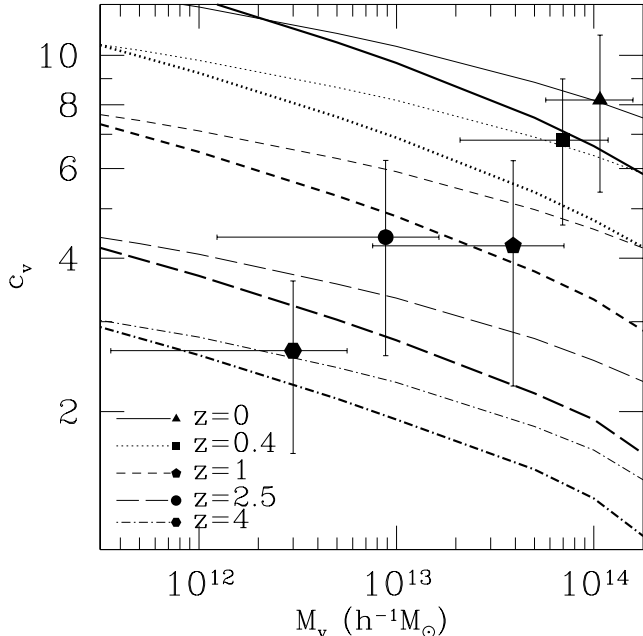


FIG. 6.— Median concentration vs. virial mass at different redshifts for the progenitors of clusters in our sample (*points*). The vertical errorbars represent the 1σ scatter in concentrations for the 14 clusters, while horizontal errorbars show the mass range of the halos at each epoch. The predictions of the Bullock et al. (2001) (*thick lines*) and the Eke et al. (2001) (*thin lines*) models are plotted for comparison.

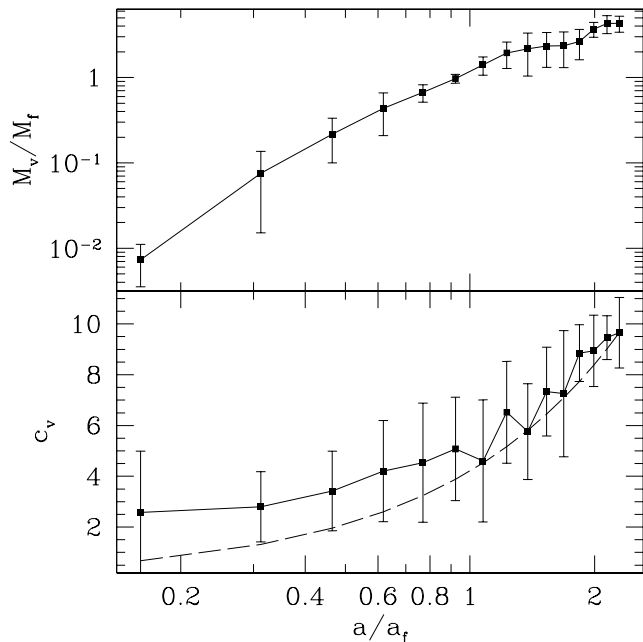


FIG. 7.— Average mass accretion history (*top panel*) and average concentration of cluster progenitors (*bottom panel*) as a function of scale factor measured in units of the formation scale factor, a_f . The errorbars in both panels represent the 1σ spread around the mean. The figure shows that the concentration is approximately constant at $c_v \approx 3-4$ during the period of rapid mass accretion ($a/a_f < 1$) and increases with decreasing redshift during the period of slow mass growth ($a/a_f > 1$). For comparison the *dashed line* shows $(1+z)^{-1}$ evolution.

have typically smaller r_s than that of the M profile. As a result, they reach their asymptotic slopes at smaller distances. An analytic profile, of course, can be a

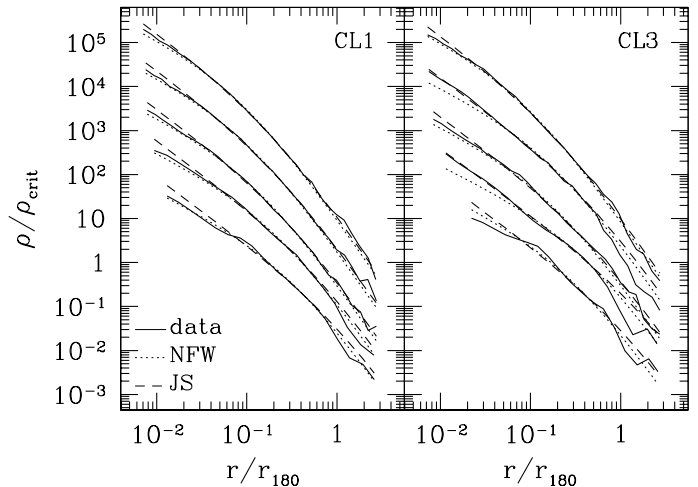


FIG. 8.— The density profile of CL1 (*left panel*) and CL3 (*right panel*) at (from top to bottom) $z = 0, 0.2, 0.4, 1,$ and 1.5 (*solid lines*). The profiles at $z > 0$ are scaled down by a factor of 10 with respect to each other. Also shown are the best fit NFW (*dotted lines*) and the JS (*dashed lines*) profiles. At all shown redshifts the NFW profile is a better fit to the simulated profile of CL1 than the JS profile. CL3 is shown as an exception to the typical behavior represented by CL1 and CL2 (Fig. 4). For CL3 the best fit at $z = 0$ (NFW) is not the best fit at earlier epochs.

the best fit analytic fits shown in the top panels of Figure 5. The only cases where the slope profiles are flat for relatively large radius ranges, correspond to the halos with recent merger activity and rapid mass growth (i.e., CL4, CL9, CL10, CL13).

Interestingly, we find that the density profiles of systems that experience intense merger activity until the present epoch (clusters CL4, 9, 10 and 13) can be well described by a single power law $r^{-\gamma}$ with slope γ ranging from -1.5 to -2 . Similarly to other profile shapes, the power law density profile for these systems is maintained for earlier epochs out to $z \sim 1.5$. In addition, there is evidence that the profiles of all clusters during their rapid mass growth stages are close to a power law. In particular, we find that the power law provides an increasingly better fit with increasing redshifts for all of our clusters. At early epochs ($z \gtrsim 1.5-2$), the power law fit is always either comparable or better than the NFW, M, and JS analytic profiles. The power law like profiles relate to low concentrations. This is because they maintain a slope slightly shallower than -2 out to large radii so that the scale radius is large. Indeed, the clusters with power law profiles at $z = 0$ have the lowest concentrations in our sample. The decrease of concentrations at higher redshifts may thus reflect the power law like density profiles of actively merging systems.

6. DISCUSSION AND CONCLUSIONS

We have studied the MAHs and density profiles of 14 cluster-size halos simulated using the ART code in a flat Λ CDM cosmology. In agreement with previous studies, we find that most MAHs have a similar shape: an early, merger-dominated mass increase followed by a more gradual, accretion-dominated growth. To obtain a formation redshift that characterizes the overall shape of the MAH we perform analytic functional fits. The typical MAHs are well described by the one parameter exponential good fit regardless of whether its inner asymptotic slope is resolved.

function proposed by W02 (Eq. [2]). Two of the clusters in our sample experience intense merger activity and rapid mass growth until the present-day epoch. The MAHs of these systems are better described by a one parameter power-law function in the scale factor. We thus generalize the form proposed by W02 into a two parameter form (Eq. [4]) to encompass both exponential and power-law MAHs. For each class, however, the fit reduces to a one parameter fit.

We check the convergence of halo density profiles using a re-simulation of one of the clusters with eight times more particles and better force resolution. We show that both the halo profiles and their local logarithmic slopes converge at scales larger than about four times the formal resolution of the low resolution run, in agreement with a previous convergence study of the ART code by Klypin et al. (2001). We fit the density distribution of the clusters with the NFW, M, and JS analytic profiles. Experiments show that the choice of merit function, weighting, and binning affect the absolute quality of a fit and may bias conclusions about how well a particular analytic profile fits simulation results. We find, however, that the relative goodness of fit for the three analytic profiles and our conclusions about the best fit profile are robust to the changes in binning and merit function.

The main general result of our study is a remarkable diversity of the mass accretion histories, profile shapes, concentrations, and inner slopes for cluster-size halos in a relatively narrow mass range. The concentrations of cluster-size halos at the present-day epoch exhibit a scatter of $\sigma_{\log c_v} \approx 0.20$. This scatter is related to the diversity of halo MAHs and formation redshifts. We find a statistically significant correlation between the formation redshift and the concentration of a halo, in agreement with results of W02. There is a more detailed connection between the MAH and concentration. The concentration of a halo is approximately constant at $c_v \approx 3-4$ during the period of rapid mass growth and frequent major mergers ($z > z_f$) and increases with decreasing redshift when the mass accretion rates slows down at $z < z_f$. This behavior was recently pointed out by Zhao et al. (2003b,a). The implied “floor” in the concentration is not accounted for in the currently used models for $c_v(M)$ (Bullock et al. 2001; Eke et al. 2001), which predict a monotonic decrease of concentration with increasing mass and may thus underestimate concentrations of the most massive, $\gtrsim 5 \times 10^{14} h^{-1} M_\odot$, halos. This may have important implications for estimates of expected number of wide-separation quasar lenses (e.g., Kuhlen et al. 2003) and other results sensitive to the concentrations of very massive clusters.

The inner logarithmic slope of cluster profiles at 3% of the virial radius (or 10–50 kpc) ranges from -1.2 to -2 . In the best resolved clusters the logarithmic slope does not seem to reach a specific asymptotic value down to the smallest resolved scales in our simulations ($r/r_{180} \simeq 0.007$). A similar conclusion was reached by Klypin et al. (2001) for galaxy-size halos and several recent studies (Power et al. 2003; Ascasibar et al. 2003; Fukushige et al. 2003; Hoeft et al. 2004; Hayashi et al. 2003). It is still not clear whether the density profiles in our simulations are consistent with density distribution of observed clusters. We note, however, that at the scales probed in observations the slope is not expected to be shallower than -1 .

The asymptotic value of the slope has been a subject of much numerical effort in the last several years. Our results indicate that a universal asymptotic slope may not exist. We should note that the resolution of current dissipationless simulations is sufficiently high to converge on the density profile at scales

smaller than the size of a typical central galaxy in clusters and groups ($\sim 30-50$ kpc). Further improvement in profile modeling should therefore include realistic dynamics and cooling of the baryonic component as contraction of gas is expected to significantly modify dark matter distribution at these scales.

One of the most interesting results of our study is existence of systems with density profiles that can be well described by a power law $\rho \propto r^{-\gamma}$ with γ ranging from ≈ -1.5 to ≈ -2 . All of these systems are still in their rapid mass growth stage and experienced a recent major or minor merger. Remarkably, these halos maintain the power law density profiles at earlier epochs out to at least $z \sim 1.5$. The relatively shallow $\gamma > -2$ power law slopes result in low concentrations as the scale radius where the density profiles reaches the slope of -2 is at large radii. There are also indications that the profiles of all clusters are power law like during their rapid mass growth stages. We find, for example, that the power law provides an increasingly better fit with increasing redshifts for all of our clusters. At early epochs ($z \gtrsim 1.5-2$), the power law fit is always either comparable or better than the NFW, M, and JS analytic profiles. We did not find any correlation of the power slope with the details of the cluster MAH. It would be interesting to look for such correlations using a larger sample of objects.

When the mass growth slows down at $z > z_f$, an outer steeper density profile is built up. As pointed out by Zhao et al. (2003b), the difference in density profiles during the two mass accretion regimes may be due to more violent and thorough relaxation during the period of rapid mass growth. Although Zhao et al. (2003b) focused on halo concentrations and did not consider density profile shapes, their results are consistent with our conclusions. In particular, they find that during the rapid mass growth stage the circular velocity is nearly constant from the scale radius to the virial radius. This behavior is consistent with a power law density distribution with a slope close to -2 .

In a recent study, Ascasibar et al. (2003) find that objects which experienced a recent merger event⁶ have lower concentrations and steeper inner profiles than more relaxed systems. This is consistent with our findings described above. At the same time, Ascasibar et al. (2003) find that relaxed systems are better fit by the NFW, while systems with a recent major or minor merger by the M profile (see also Ascasibar 2003). They thus associate a particular shape of the profile with a recent merger history. In contrast, our results show the shape of density profiles is set early in the halo evolution and is usually stable over the past ten billion years. Clusters with density profiles best described by the NFW rather than a JS at $z = 0$, tend to have NFW-like profiles at earlier epochs as well. The reverse is also true. We tested this conclusion using the high-resolution re-simulation of one of the clusters in our sample. Also, we do not find any correlation between the redshift of last major merger (in our definition) or the formation redshift and the best fit analytic profile.

The origin of the distinctive density profile shape of the CDM halos remains poorly understood. Our results and results of other recent studies indicate that the shape is tightly linked to the halo mass accretion history. During the period of rapid mass accretion the violent relaxation is significant and results in a power-law like density distribution. This stage of evolu-

⁶ Note that Ascasibar et al. (2003) identify a recent merger by the presence of massive substructures within virial radii of their systems. This is different from our definition, which identifies major mergers directly from mass accretion tracks.

tion usually occurs early when the universe is dense and builds up the inner dense regions of halo. At this point, the logarithmic slope of the density distribution is shallower than -2 over a large fraction of the halo volume and its concentration is small. At later epochs, as the mass accretion rate slows down, the outer regions of the halo are built while its central regions remains nearly intact. This can be seen in Figure 8 and Figures 10-13 of Fukushige & Makino (2001). This picture can explain why the best fit analytic profiles tend to be the same at various redshifts. The fits are sensitive to the density distribution at small and intermediate ($\sim r_s$) radii which are set early. However, it is still unclear which process(es) determines a particular shape of the profiles. The key to understanding these processes appears to be in the details of early evolutionary stages of CDM halos, which will be the subject of a future study.

We would like to thank Tony Tyson for stimulating discussions which motivated this study, and Risa Wechsler for a careful reading of the draft and many useful comments and suggestions. This work was supported by the National Science Foundation (NSF) and NASA under grants No. AST-0239759 (CAREER) and NAG5-13274, by the NSF Center for Cosmological Physics (CfCP) at the University of Chicago, and by the NSF grant AST-0206216 at NMSU. We would like to thank NSF/DAAD for supporting our collaboration. The simulations were performed at the Leibniz Rechenzentrum Munich and the John von Neumann Institute for Computing Jülich.

REFERENCES

- Allen, S. 1998, MNRAS, 296, 392
 Arabadjis, J., Bautz, M., & Garmire, G. 2002, ApJ, 572, 66
 Ascasibar, Y. 2003, astro-ph/0305250
 Ascasibar, Y., Yepes, G., Müller, V., & Gottlöber, S. 2003, MNRAS submitted, astro-ph/0306264
 Athreya, R., Mellier, Y., van Waerbeke, L., et al. 2003, A&A, 384, 743
 Avila-Reese, V., Firmani, C., Klypin, A., & Kravtsov, A. V. 1999, MNRAS, 310, 527
 Bautz, M. & Arabadjis, J. 2003, astro-ph/0303313
 Blais-Ouellette, S., Amram, P., & Carignan, C. 2001, AJ, 121, 1952
 Broadhurst, T., Huang, X., Frye, B., & Ellis, R. 2000, ApJ, 534, L15
 Bullock, J. S., Kolatt, T. S., Sigad, Y., Somerville, R. S., Kravtsov, A. V., Klypin, A. A., Primack, J. R., & Dekel, A. 2001, MNRAS, 321, 559
 Côté, S., Carignan, C., & Freeman, K. C. 2000, AJ, 120, 3027
 Clowe, D., Luppino, G., Kaiser, N., & Gioia, M. 2000, ApJ, 539, 540
 Clowe, D. & Schneider, P. 2001, A&A, 379, 384
 Colin, P., Klypin, A., Valenzuela, O., & Gottlöber, S. 2003, ApJ submitted, astro-ph/0308348
 Czoske, O., Moore, B., Kneib, J.-P., & Soucaill, G. 2002, A&A, 386, 31
 de Blok, W. J. G., Bosma, A., & McGaugh, S. 2003, MNRAS, 340, 657
 de Blok, W. J. G., McGaugh, S. S., & Rubin, V. C. 2001, AJ, 122, 2396
 Diemand, J., Moore, B., Stadel, J., & Kazantzidis, S. 2003, MNRAS submitted, astro-ph/0304549
 Dolag, K., Bartelmann, M., Perrotta, F., Baccigalupi, C., Moscardini, L., Meneghetti, M., & Tormen, G. 2003, astro-ph/0309771
 Dubinski, J. & Carlberg, R. G. 1991, ApJ, 378, 496
 Eke, V. R., Navarro, J. F., & Steinmetz, M. 2001, ApJ, 554, 114
 Evrard, A. E., Metzler, C. A., & Navarro, J. F. 1996, ApJ, 469, 494
 Flores, R. A. & Primack, J. R. 1994, ApJ, 427, L1
 Frenk, C. S., White, S. D. M., Efstathiou, G., & Davis, M. 1985, Nature, 317, 595
 Fukushige, T., Kawai, A., & Makino, J. 2003, astro-ph/0306203
 Fukushige, T. & Makino, J. 1997, ApJ, 477, L9
 —. 2001, ApJ, 557, 533
 —. 2003, ApJ, 588, 674
 Gavazzi, R., Fort, B., Mellier, Y., Pello, R., & Dantel-Fort, M. 2002, astro-ph/0212214
 Ghigna, S., Moore, B., Governato, F., Lake, G., Quinn, T., & Stadel, J. 2000, ApJ, 544, 616
 Gottlöber, S., Klypin, A., & Kravtsov, A. V. 2001, ApJ, 546, 223
 Hayashi, E., Navarro, J. F., Power, C., Jenkins, A., Frenk, C. S., White, S. D. M., Springel, V., Stadel, J., & Quinn, T. 2003, ApJ submitted, astro-ph/0310576
 Hoefl, M., Mückel, J., & Gottlöber, S. 2004, ApJ accepted, astro-ph/0311083
 Hu, W. & Kravtsov, A. V. 2003, ApJ, 584, 702
 Ibata, R., Lewis, G. F., Irwin, M., Totten, E., & Quinn, T. 2001, ApJ, 551, 294
 Jing, Y. & Suto, Y. 2000, ApJ, 529, L69
 Jing, Y. P. 2000, ApJ, 535, 30
 Klypin, A. & Holtzman, J. 1997, astro-ph/9712217
 Klypin, A., Kravtsov, A., Bullock, J., & Primack, J. 2001, ApJ, 554, 903
 Klypin, A., Kravtsov, A. V., Valenzuela, O., & Prada, F. 1999, ApJ, 522, 82
 Klypin, A., Maccio', A. V., Mainini, R., & Bonometto, S. A. 2003, ApJ submitted, astro-ph/0303304
 Kravtsov, A. V., Klypin, A. A., Bullock, J. S., & Primack, J. R. 1998, ApJ, 502, 48
 Kravtsov, A. V., Klypin, A. A., & Khokhlov, A. M. 1997, ApJS, 111, 73
 Kuhlen, M., Keeton, C. R., & Madau, P. 2003, ApJ submitted, astro-ph/0310013
 Lacey, C. & Cole, S. 1993, MNRAS, 262, 627
 Moore, B. 1994, Nature, 370, 629
 Moore, B., Ghigna, S., Governato, F., Lake, G., Quinn, T., Stadel, J., & Tozzi, P. 1999a, ApJ, 524, L19
 Moore, B., Governato, F., Quinn, T., Stadel, J., & Lake, G. 1998, ApJ, 499, L5
 Moore, B., Quinn, T., Governato, F., Stadel, J., & Lake, G. 1999b, MNRAS, 310, 1147
 Mückel, J. & Hoefl, M. 2003, A&A, 404, 809
 Navarro, J., Frenk, C., & White, S. 1996, ApJ, 462, 563
 —. 1997, ApJ, 490, 493
 Navarro, J. F., Hayashi, E., Power, C., Jenkins, A., Frenk, C. S., White, S. D. M., Springel, V., Stadel, J., & Quinn, T. R. 2003, MNRAS submitted, astro-ph/0311231
 Navarro, J. F. & Steinmetz, M. 1997, ApJ, 478, 13
 —. 2000, ApJ, 538, 477
 Power, C., Navarro, J. F., Jenkins, A., Frenk, C. S., White, S. D. M., Springel, V., Stadel, J., & Quinn, T. 2003, MNRAS, 338, 14
 Quinn, P. J., Salmon, J. K., & Zurek, W. H. 1986, Nature, 322, 329
 Sand, D. J., Treu, T., & Ellis, R. S. 2002, ApJ, 574, L129
 Sand, D. J., Treu, T., Smith, G. P., & Ellis, R. S. 2003, ApJ submitted, astro-ph/0309465
 Sheldon, E. et al. 2001, ApJ, 554, 881
 Springel, V., Yoshida, N., & White, S. D. M. 2001, New Astronomy, 6, 79
 Swaters, R. A., Madore, B. F., van den Bosch, F. C., & Balcells, M. 2003, ApJ, 583, 732
 Tyson, J., Kochanski, G., & Dell'Antonio, I. 1998, ApJ, 498, L107
 van den Bosch, F. 2002, MNRAS, 331, 98
 van den Bosch, F. C. & Swaters, R. A. 2001, MNRAS, 325, 1017
 Wechsler, R., Bullock, J., Primack, J., Kravtsov, A., & Dekel, A. 2002, ApJ, 568, 52
 Willick, J. & Padmanabhan, N. 2000, astro-ph/0012253
 Zhao, D. H., Jing, Y. P., Mo, H. J., & Boerner, G. 2003a, astro-ph/0309375
 Zhao, D. H., Mo, H. J., Jing, Y. P., & Börner, G. 2003b, MNRAS, 339, 12

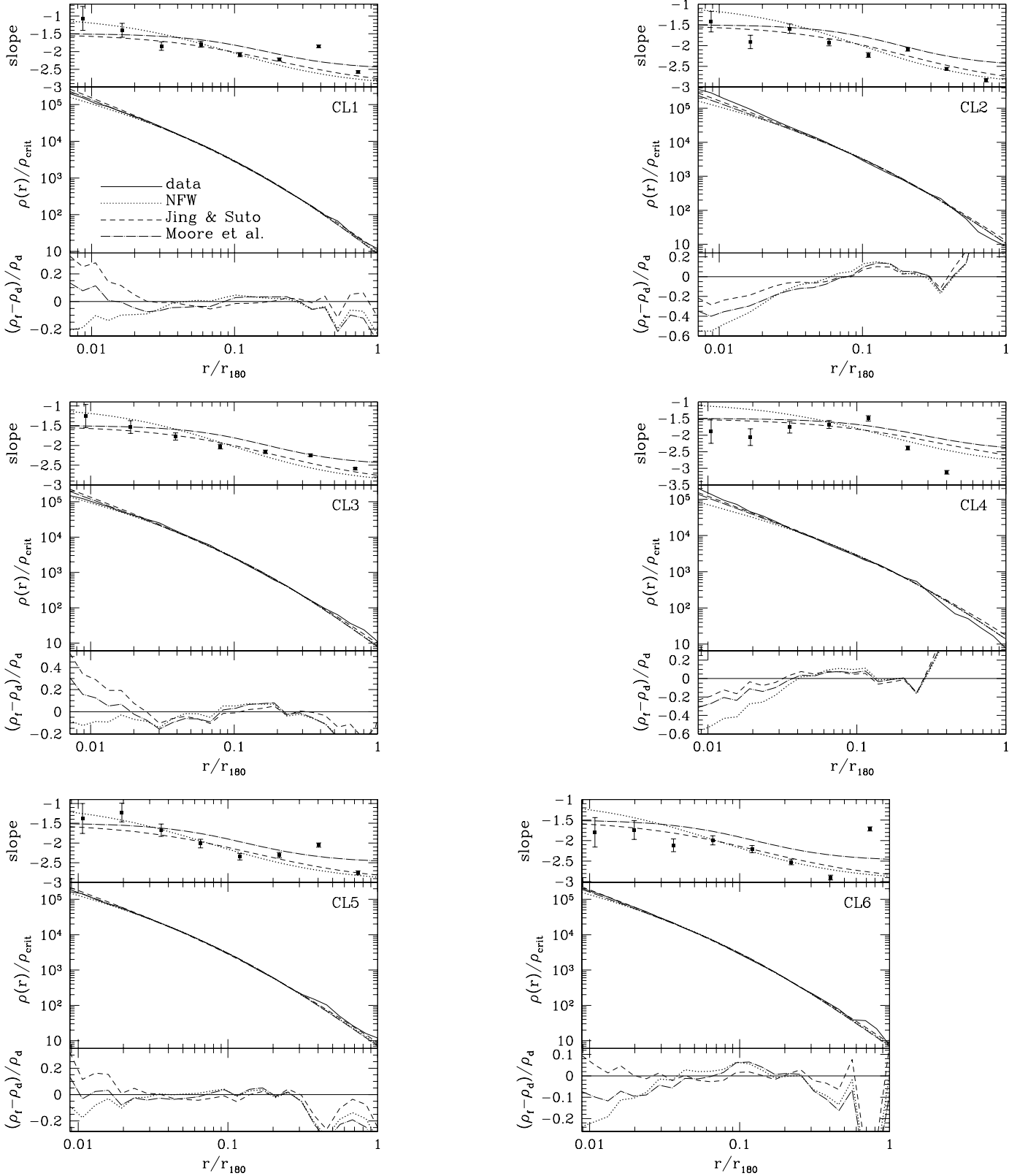


FIG. 5.— *Middle panel*: fits of the NFW (dotted curves), the Jing and Suto (short-dashed curves), and the Moore et al. (dot-dashed curves) profiles to the density distribution of the clusters of our sample at $z = 0$. The fits were done using the range $[r_{\text{min}}, r_{500}]$ and a χ^2 merit function (see §5.1 for details). The way the choice of merit function changes the fits can be seen in Figure 2. *Bottom panels*: deviations of each one of the fits (ρ_f) from the actual profile (ρ_d). *Top panels*: local logarithmic slope as a function of radius for the 3 fits. The points correspond to the local slope as derived from the actual profile.

